ADVANCED ELECTRONIC MATERIALS
www.advelectronicmat.de

Structural Anisotropy in Stretchable Silicon

Sabrina M. Curtis, Randy P. Tompkins, Barbara M. Nichols, Milena B. Graziano, Iain Kierzewski, Gabriel Smith, Marina S. Leite, and Nathan Lazarus*

Patterned planar silicon (Si) semiconductor structures able to conform around 3D surfaces are promising candidates for wearable devices from solar cells to displays. Despite the known anisotropic material properties of crystalline semiconductors, prior evaluations have assumed isotropic stretchable mechanical behavior. The effect of structural anisotropy on the mechanical stretching behavior of {100} single crystalline Si planes is demonstrated through models and experiments. 3D finite element analysis results show serpentines fabricated and strained loaded on the dense {111} family of planes will have maximum von Mises peak stresses that are 20% higher than those fabricated in the <100> direction on the {100} family of planes. A fabrication process is presented to release in-plane Si serpentine test structures from (100) silicon-on-insulator wafers aligned parallel to the <110> and <100> crystallographic orientations. The released test structures can accommodate strains to 84%. Raman spectroscopy is used to characterize anisotropic effects on the internal stresses of Si serpentines. Raman measurements confirm two different maximum stress locations on <110> and <100> Si serpentines, resulting in two different break locations. All results show anisotropy plays a critical role in the mechanical behavior of stretchable Si serpentines and must be considered during design of stretchable semiconductor structures.

1. Introduction

Wearable electronics must be able to withstand repeated large levels of external strain loading (30–100%) to match the performance of human skin without undergoing mechanical failure in the form of cracking, curling, or fatigue.[1–3] This is especially challenging, as most active electronic components in wearable devices are comprised of inorganic materials, characterized for being brittle with low intrinsic tensile strains (<1%). Yet, through mechanical design, it is possible to incorporate them into stretchable systems that can reach large global elastic strains (>100%). The "island bridge"[4,5] design, which utilizes inactive materials for stretchable connections, has demonstrated several functional wearable smart electronics including photovoltaic arrays,[6] temperature sensors,[7] electronic skin for smart surgical gloves,[8] and bioinspired digital cameras.[9] The active device surface area in this design can be increased by patterning and micromachining the semiconductors directly into stretchable structures, which allows the active device semiconductor component itself to accommodate large amounts of strain. Serpentine structures are advantageous for rigid metal and brittle semiconductor stretchable electronics due to their ability to elastically deform by tens of percent without damage through both in-plane (2D) stretching, and out-of-plane (3D) buckling. Several studies have demonstrated the mechanical stretching performance of serpentine structures depends on their geometrical dimensions[10–15] and elastomer substrate properties.[16,17] Selective area growth methods have realized serpentine-like stretchable nanowires from several popular semiconductors, including silicon (Si)[18,19] and gallium nitride (GaN).[20,21] Alternatively, dry plasma etching techniques have been successful for patterning and transferring in-plane Si serpentines[14] and AlGaN/GaN heterostructures in serpentine-like stretchable geometries[22] onto elastomer substrates.

While these methods are suitable for many stretchable applications, fabrication of high area density stretchable inorganic materials from planar substrates remains an important challenge.[23] Patterned and thru-etched semiconductors are a particularly promising approach for creating very high density, large area stretchable systems. One potential application is the creation of geometries with a global negative Poisson's

S. M. Curtis, Dr. M. B. Graziano
Oak Ridge Associated Universities Fellowship Program
US Army Research Laboratory
2800 Powder Mill Rd., Adelphi, MD 20783, USA
E-mail: scurtis@terpmail.umd.edu

S. M. Curtis, I. Kierzewski, Prof. M. S. Leite
Department of Materials Science and Engineering
University of Maryland
College Park, MD 20740, USA

Dr. R. P. Tompkins, Dr. B. M. Nichols,
G. Smith, Dr. N. Lazarus
Sensors and Electron Devices Directorate
US Army Research Laboratory
2800 Powder Mill Rd., Adelphi, MD 20783, USA

I. Kierzewski
General Technical Services LLC
3100 138 Wall, NJ 07719, USA

Prof. M. S. Leite
Institute for Research in Electronics and Applied Physics
University of Maryland
College Park, MD 20740, USA

The ORCID identification number(s) for the author(s) of this article can be found under https://doi.org/10.1002/aelm.201900003.

DOI: 10.1002/aelm.201900003

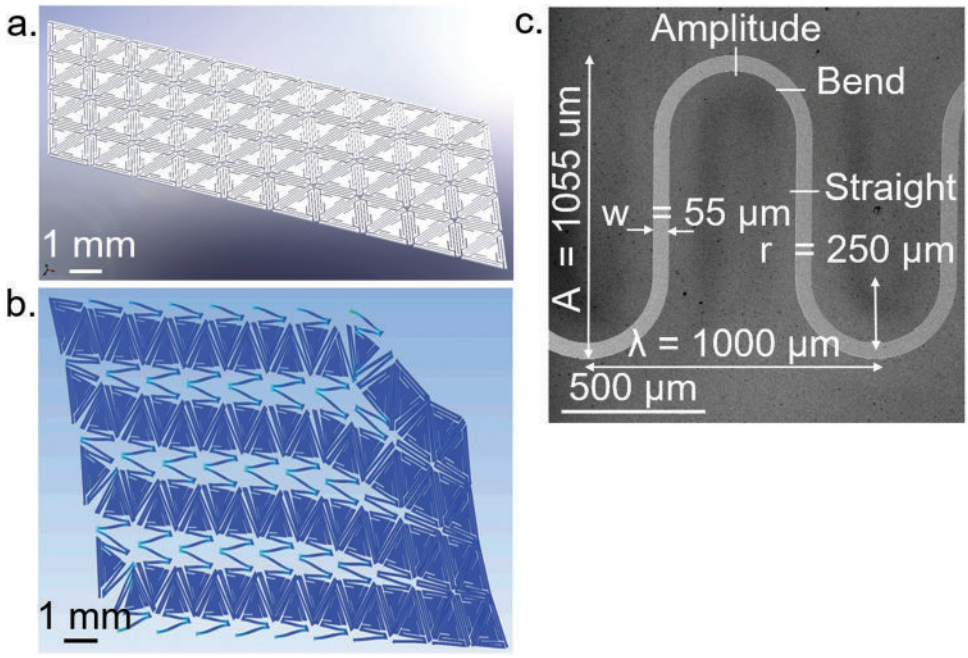

Figure 1. Schematic cell design of synclastic stretchable structure using in-plane Si serpentine interconnects. a) Illustration of large area stretchable synclastic structure with an 80% surface area coverage. b) FEA results showing Si fracture at 50% external strain. c) Serpentine geometrical dimensions (width (w), radius (r), peak-to-peak amplitude (A), wavelength (λ)) and three critical segment positions (amplitude, bend, straight) defined on a SEM image of a serpentine evaluated in this study.

ratio known as auxetic mechanical structures.[24] Semiconductor auxetic mechanical structures can readily display synclastic bending over dome-shaped curvatures,[25] which makes them ideal candidates for high area coverage applications such as deformable inorganic solar cell tarps.[26] Microelectromechanical systems (MEMS) processing techniques can be used to pattern crystalline semiconductors into both islands and serpentine interconnect to form a mechanically resilient geometry.[27,28] **Figure 1**a shows an illustration of a synclastic Si structure composed of serpentine interconnects. Finite element analysis (FEA) results in Figure 1b indicate Si fabricated into this structure could hold a surface area coverage of 80% at equilibrium, where only 20% of the Si is etched, while elastically recovering from a 50% global strain when stretched. Design of the serpentine interconnect's geometrical dimensions (wavelength (λ), peak-to-peak amplitude (A), width (w), thickness (t), radius (r)) within the auxetic structure allows one to engineer a tunable stretchable inorganic semiconductor with enhanced surface area coverage and increased stretchability. Furthermore, it is possible to anisotropically strain engineer the serpentine's crystallographic orientation through mask design in such a structure. This is especially critical as structural anisotropy plays a significant role on the stretchable performance of crystalline semiconductor–based devices. Figure 1c shows a scanning electron microscopy (SEM) image labeling the relevant geometrical parameters (λ, A, w, t, r) and segment positions (amplitude, bend, and straight) on a curved corner serpentine interconnect analyzed in this study.

Organic semiconductor–based stretchable systems are reported to display anisotropic optical, thermal, electrical, and mechanical performance with strain direction.[29–31] While the thermal and optical properties of Si are isotropic, elastic anisotropy becomes important under loading conditions.[32] Single crystal Si is known to display anisotropic fracture modes and strength distributions. For example, the fracture strength of <110> Si is reported to diverge between $\sigma_f = 0.6 - 1.2$ GPa.[33] Huang et al. provides a detailed experimental study using X-ray imaging and scattering on single crystal Si loaded along two different crystal directions to attribute this divergence to Si's anisotropic fracture modes.[33] They found easy crack propagation with cleavage-induced fracture on Si {111} and {110} planes when strain loaded along the <110> direction.[33] Another FEA study found that a <100> Si cube could axially displace close to 30% higher and 3× larger than a <110> cube. However, they observed near isotropic mechanical performance for <110> Si cubes, and recommended aligning applied loads along this direction.[32]

Prior studies of anisotropy in stretchable inorganic semiconductors are limited to computational modeling, most likely due to limitations in fabrication schemes and available stretchable stress characterization techniques. While an anisotropic dependence of buckled Si on pre-strained substrates was observed, past modeling efforts assumed isotropic linear mechanical behavior.[15] J. Song experimentally and mathematically demonstrated maximum wrinkle growth rate of Si thin-films align along the [100] direction, because this orientation has the lowest critical buckling stress in the Si cubic structure.[34] With a 2D FEA solver, Tompkins et al. found the maximum von Mises peak stresses could vary by 17% within the (100) Si plane after applying 30% global strain to the serpentine along various crystal directions.[35] For a Si serpentine–based structure, the Young's modulus is an anisotropic property

reflected in Si serpentine interconnects by in-plane rotations of the elastic stiffness tensor.[36] Anisotropic variations in the elastic properties of crystalline semiconductors are expected to directly affect stretchable device's global stretching performance such as the maximum strain-to-rupture (end-to-end displacement) and fracture location along the serpentine trace.

Here, the influence of crystalline anisotropy on the mechanical stretching performance of in-plane Si serpentine interconnects is demonstrated through combined 3D FEA, fabrication, tensile testing, and micro-Raman spectroscopy (μRS) experiments. FEA modeling results predict Si <100> (100) serpentines can reach larger maximum displacements than Si <110> (100) serpentines and Si (111) serpentines. Modeling results also predict maximum stress concentration and subsequent serpentine fracture is orientation dependent, occurring on the position of the arc that intersects the common slip <110> direction. To confirm these results, a fabrication and release procedure is developed to build Si (100) serpentine mechanical test structures aligned along the <110> and <100> crystallographic directions for stress measurements using μRS.

The linear correlation between shifts in the Raman spectra and amount of stress in crystalline materials is well defined for Si,[37–40] with examples of direct stress measurements on Si microcapsules[41] and Si bridges.[42] Raman can also be used to measure stress in III–V semiconductors such as AlN and GaN,[43] and other zinc blend type semiconductors including Ge, GaAs, GaSb, InAs, and ZnS.[44] For Si to be reliable when implemented into stretchable devices, we must understand anisotropic effects on the materials' cyclic fatigue performance. Therefore, we show μRS can be a very useful tool in characterizing localized stress, and thus crystalline anisotropy in semiconductors during external straining measurements.

2. Results and Discussions

2.1. Finite Element Analysis Anisotropic Evaluation

The position and value of maximum stress (σ) after an applied external strain (ε) is evaluated for serpentines fabricated on the relevant Si (100) and Si (111) MEMS planes, using Hooke's law ($\sigma = \varepsilon C_{ijkl}$). Owing to the lack of inversion symmetry of Si's diamond cubic crystal structure (**Figure 2**a), the Young's modulus of Si is an anisotropic property known to vary by 45% ($E_{<111>} = 188$ GPa, $E_{<110>} = 169$ GPa, and $E_{<100>} = 130$ GPa) with crystal orientation.[36,45] Expanding on the study by Tompkins et al.[35] using a 3D FEA solver which allows for out-of-plane deformation modes, we represent in-plane crystalline anisotropy on Si serpentines by solving for the elastic stiffness tensor (C_{ijkl}) for various in-plane crystal orientations. The first elastic

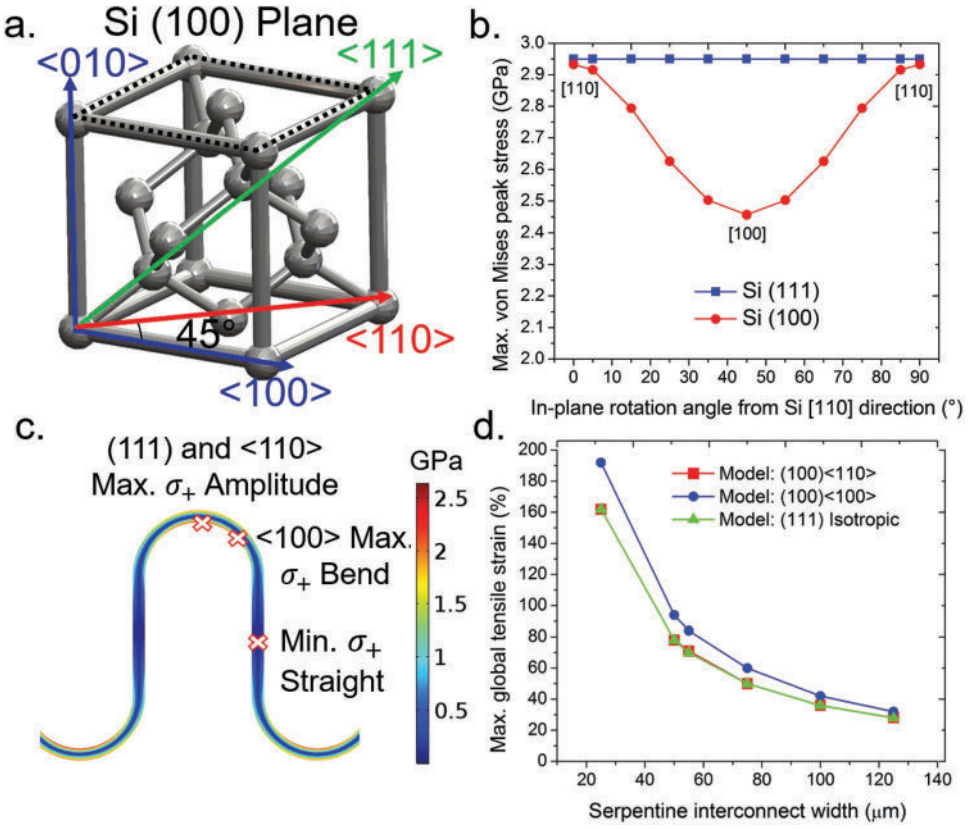

Figure 2. Si anisotropic effects on serpentine stretchable behavior. a) Illustration of the <110>, <100>, <111> directions and (100) plane on the diamond cubic crystal structure of Si. b) Maximum von Mises peak stress (σ_+) as a function of in-plane rotation angle on Si (100) and (111) for a 55 μm wide serpentine, after an applied 30% strain parallel to the trace. c) Serpentine stress distribution showing fracture occurs at the apex of the amplitude for Si (111) and (100) <110> and on the bend for (100) <100> serpentines. d) Influence of anisotropy on the maximum global tensile strain of serpentines on Si (111) plane and Si (100) plane in the <110> and <100> directions, as a function of serpentine interconnect width.

stiffness coefficient (C_{11}) is shown in Figure S1a in the Supporting Information for in-plane rotations (in 5°–10° increments) about the [110] direction on a (100) Si wafer. Within the (100) Si plane, the <100> family of directions have the lowest C_{11} coefficient and are expected to be the most mechanically complaint family of directions, and the <110> family of directions have the stiffest C_{11} coefficient. The <100> directions are 45° in-plane rotation away from the traditional wafer flat parallel to the <110> family directions, as labeled on a standard (100) Si wafer in Figure S1b in the Supporting Information.[36,45,46]

The dense Si (111) plane displays an in-plane isotropic Young's modulus at $E = 169$ GPa. The stiffest Young's modulus in Si occurs normal to this plane, along the <111> direction at $E = 188$ GPa. Since the elastic moduli on Si (111) closed packed plane are well-known to be rotationally independent,[47] we use the COMSOL model's built-in Si isotropic materials properties to represent Si (111). The material's properties (Young's modulus, Poisson's ratio, and shear modulus) of Si (100) and (111) planes are given in Table I in the Supporting Information.[48] The elastic stiffness matrix of the <110> and <100> directions is given in Equations S1 and S2 in the Supporting Information. A detailed description of mechanical anisotropic material properties for Si is given in ref. [48].

We first model a $\varepsilon = 30\%$ uniaxial global strain applied parallel to the length of 5-period serpentines. Global strain is defined as $\varepsilon = \Delta L/L$, where L is defined as the initial end-to-end length and ΔL is the change in the length. Figure 2b shows the maximum von Mises peak stress on serpentines after a 30% global strain, when patterned at different in-plane angles on Si (100) and Si (111) wafers. Serpentines fabricated on the dense Si (111) plane are found to have stresses 20% higher than those fabricated from the (100) plane. Anisotropy within Si (100) plane also causes the maximum von Mises peak stress to be 20% higher when serpentines are strain loaded in the <110> direction of Si compared to those fabricated parallel to the <100> direction. The stresses are nearly the same between the <110> (100) and <110> (111) most likely because the stiff <110> direction is the cleavage direction for Si.[49] These 3D FEA results suggest serpentines patterned and stretched on the Si (100) plane along the <100> direction can reach larger global strains than Si (100) <110> and (111) serpentines.

Consistent with prior Si serpentine modeling reports, the curved corner geometry is found to gradually distribute stress over the entire arc of each period which results in low stress under applied external strain.[15] Anisotropy is also found to dictate the position of maximum stress and subsequent fracture location on serpentine semiconductor devices. As shown in Figure 2c, serpentines fabricated from the isotropic Si (111) plane are found to concentrate stress and subsequently fracture at the apex of the amplitude along the <110> direction at a 90° angle from the direction of strain loading. Serpentines fabricated from the Si (100) plane and strain loaded along the <110> direction are also found to break at the same direction and location. However, Si (100) serpentines parallel to the <100> direction are predicted to break off-center of the arc (bend) at the position which intersects the <110> direction at a 45° angle. The different serpentine fracture locations on Si (100) are labeled in the stress distribution in Figure 2c, and will be experimentally verified later.

We then evaluate anisotropic effects on the maximum global tensile strain of identical Si serpentines strain loaded along different crystal orientations as a function of trace width (w). The maximum global tensile strain is the maximum end-to-end displacement before serpentine fracture. In simulation studies, Si failure was determined when the maximum von Mises peak stress in the serpentine structure exceeds the material's yield stress ($\sigma_y = 6.9$ GPa).[50] Figure 2d shows the maximum global tensile strain of serpentines fabricated and stretched along the <110> and <100> directions on the Si (100) plane, and Si (111) plane, as the trace width is increased from 25 to 125 μm. Serpentines strain loaded on Si (111) and <110> (100) are predicted to reach the same maximum end-to-end displacement, which is modeled to be 14–21% lower than <100> (100) serpentines. Decreasing the serpentine's width/thickness reduces the effective bending stiffness of the structure thus enabling flexibility and out-of-plane deformation. Serpentines with a width of 25 μm are simulated to achieve maximum end-to-end displacements of up to 192% primarily through out-of-plane buckling deformation which results in nonuniform straining profiles.[14] In contrast, as width/thickness are increased the structures become stiff, more restricted to in-plane movement, thus achieve lower overall global tensile strains In this study we experimentally analyze serpentines ($t = 7$ μm, $w = 55$ μm) strained loaded along the <110> and <100> orientations. Simulation results predict <110> serpentines will reach maximum strains of 72% whereas identical <100> serpentines can reach maximum strains of 84%.

2.2. Serpentine Fabrication and Tensile Testing

2.2.1. Si Serpentine Fabrication

As the models have shown, it is possible to demonstrate elastic anisotropic effects within a Si serpentine. These simulations will be experimentally verified via tensile testing and stress characterization with μRS. **Figure 3**a–d shows the fabrication procedure developed for in-plane Si serpentine mechanical test structures from (100) silicon-on-insulator (SOI) wafers. The photomask is designed to include Si serpentines along the <110> direction parallel and perpendicular to the wafer flat, as well as in the <100> direction, a 45° rotation from the wafer flat. Si serpentine structures are fabricated with the following dimensions: 5 periods, 1 mm peak-to-peak amplitude (A), 1 mm wavelength (λ), 55 μm width (w), 250 μm arc radius (r), and a thickness of 7 μm (t). The thickness of the top Si device layer of the SOI determines the deformation buckling mode of the serpentine, where a $\left(1 > \frac{t_{Si}}{w_{Si}}\right)$ is expected to result in wrinkling and/or out-of-plane buckling deformation.[14]

Since handling a silicon layer below 100 μm thickness is difficult, we utilize a 3 × 7 mm mechanical support frame around each released serpentine which was kept the full thickness of the handle wafer. The structure is released through a series of dry plasma etches with inductively coupled plasma reactive ion etching (ICP-RIE) and the Bosch process (deep reactive ion etching [DRIE]). An SEM image of the final fully released Si serpentine is shown in Figure 3f. The authors predict with

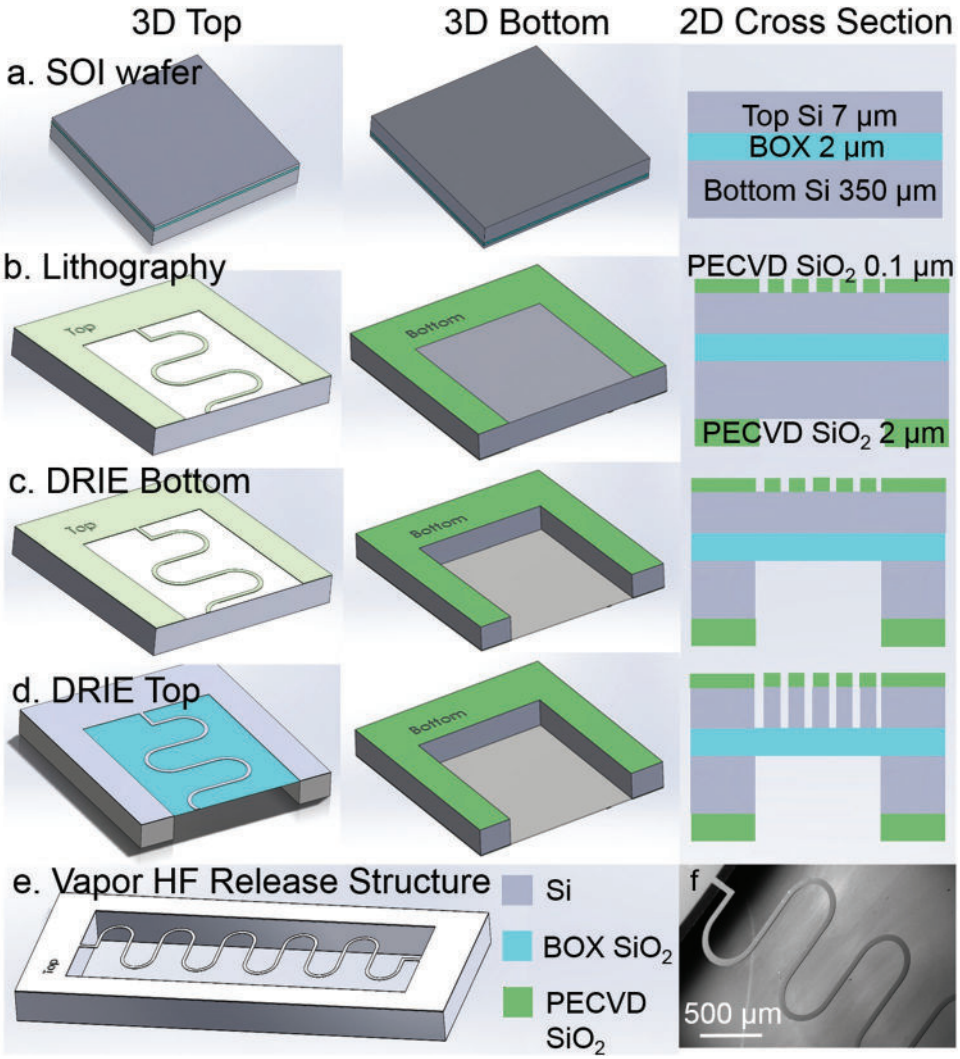

Figure 3. Microfabrication procedure of in-plane stretchable single crystal Si microstructures. a) Starting material of SOI wafer piece part with a cross section of 7 µm top Si device/3 µm buried oxide layer (BOX)/350 µm bottom Si handle. b) Photolithography to pattern the bottom Si side with 2 µm thick SiO_2 hard mask, to define a mechanical support structure. Backside alignment is used to pattern the top Si with a 0.1 µm SiO_2 hard mark, consisting of both the frame and suspended serpentine pattern in the respective orientation. c) The piece is fixed to a carrier wafer, and DRIE bottom Si handle side until the BOX layer is exposed. Dielectric ICP-RIE etch buried oxide. d) Piece fixed to carrier wafer, DRIE top device side to define serpentine structure. e) Final released structure cleaned with vapor hydrofluoric acid (HF). f) SEM image of fabricated curved corner test structure ($w = 55$ µm).

slight etch modifications, these fabrication procedures can be adapted to produce in-plane serpentines from patterned (111) SOI, polycrystalline SOI, and other epitaxially grown semiconductors on double side polished Si/SOI substrates. However, experimental demonstration of serpentines from these types of substrates is beyond the scope of this work.

2.2.2. Serpentine Tensile Testing

We experimentally characterize anisotropic effects on stretching performance of (100) Si serpentines through uniaxial tensile tests. These took place with a 3D-printed custom-built sample holder, designed to allow serpentine straining during Raman measurements. This holder is described in the experimental methods section and is shown in Figure S2 in the Supporting Information. **Figure 4** demonstrates the global and local experimental and modeling results of a 5 mm long serpentine compressed, at equilibrium and in tension along the <110> direction. Figure 4a shows the serpentine compressed to a global end-to-end displacement of 3.8 mm, −24% its original length. Figure 4b displays the serpentine pulled back to equilibrium at 5 mm, 0%. Figure 4c demonstrates the experimental strain to fracture was at 9.2 mm (84%), which is 15% larger than the model's predictions of a maximum strain at 8.6 mm (72%). Due to the thin cross section of the serpentine, under applied external strain the structure is susceptible to undergo buckling and twisting deformation, which most likely is the reason the experimental displacement in Figure 4c is slightly larger than predicted by the model.[23]

The twisting and buckling deformation results in a nonuniform experimental displacement profile. The periods on either

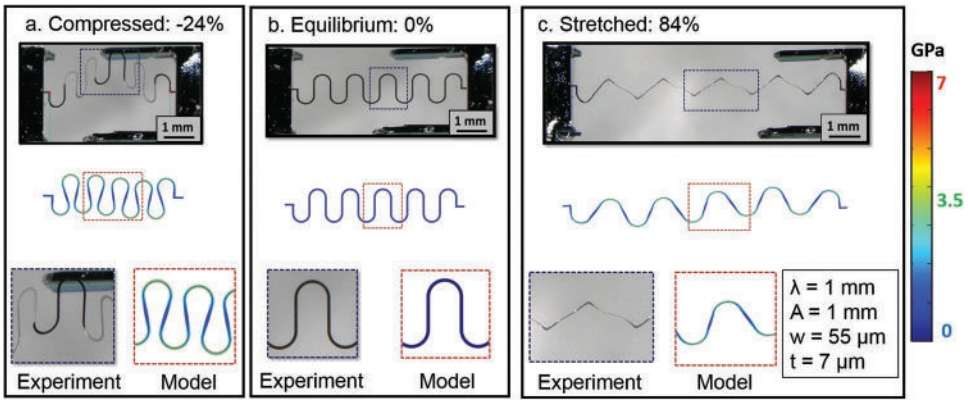

Figure 4. Experimental and model comparison of <110> Si serpentine uniaxial tensile tests. Global and local Si serpentine straining behavior: experimental (blue) and model (red). Frame a) serpentine compressed to −24% (3.8 mm) through out-of-plane flexing deformation. Frame b) serpentines unstretched at equilibrium 0% (5 mm). Frame c) serpentine experimental fracture at 84% (9.2 mm) and model fracture at 72% (8.6 mm).

end of trace connected to the mechanical frame are somewhat clamped which causes the local strain within the middle periods to be larger than the end-to-end external strain. Therefore, in our analysis we only consider the three middle serpentines periods that are unrestricted in movement. We examine anisotropic effects on the global and local strain displacement profile of buckled serpentines strain loaded in the <110> and <100> directions in **Figure 5**a,b. The experimental displacement profiles is shown for a <110> serpentine at a global strain of 49% and a <100> serpentine at a global strain of 58%. The row below each optical image shows the corresponding model, magnified by a factor of 2. The global experiments and models are shown at a 30° tilt to clearly show the similarities in the buckling behavior, where one straight segment remains rigid and the other two buckle twice. A similar buckling profile was reported for a 10 μm thick in-plane copper curved corner serpentine.[14] The blue and red frame inserts show the local displacement profile of the experiments and models, respectively. The local model is magnified by a factor of 5 to clearly show FEA results predicts maximum stress concentration at the same regions shown in the experiment.

Since there are minor inconsistencies between the displacement profile of the experiment and model of <110> and <100> serpentines, we evaluate changes in the middle three local period's peak-to-peak amplitude (A), and wavelength (λ) in Figure S3 in the Supporting Information. In this figure we annotate the local displacements in the top-down view (0°) image and show the corresponding titled-view (30°) of each deformed serpentine interconnect to clearly show the buckled deformation. For the <110> serpentine, the peak-to-peak amplitude (A) varies between 704 and 800 μm and the wavelength (λ) varies between 1572 and 1697 μm. In comparison the corresponding <110>

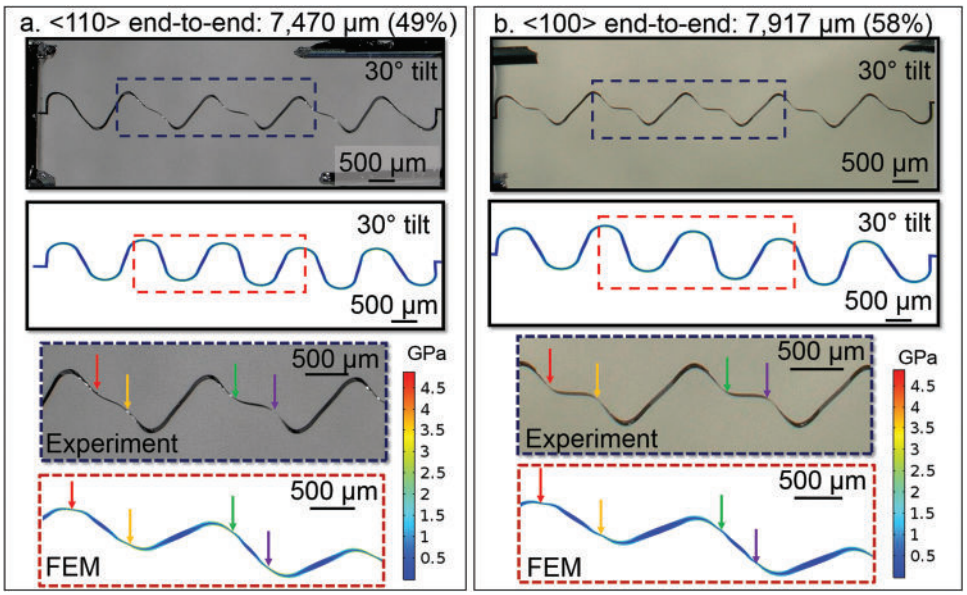

Figure 5. Model and experimental buckling analysis of Si serpentines strain loaded along the <110> and <100> direction. Optical micrographs and model comparison of the nonuniform straining profile of a) <110> serpentine held at a global strain of 49% and b) <100> serpentine held at a global strain of 58%. The model and experiment are shown at a titled 30° angle to show serpentine buckling behavior. The model is magnified by a factor of 2× globally, and 5× locally to show accurate predictions of buckling behavior at the regions demonstrated by the experiment, indicated by the colored arrows.

3D FEA predicts A = 949–969 μm and λ = 1451–1529 μm. The <100> experiment serpentine shows A = 680–686 μm, and λ = 1667–1687 μm, whereas 3D FEA predicts A = 943–971 μm, and λ = 1547–1612 μm. All measurements were taken using the program image J, which gives a potential error of +/−50 μm which corresponds to a 0.5% error for global strain measurements and up to 5% error for local strain measurements. In general, deformation between the amplitudes and wavelengths of the simulations and experiments are in reasonable agreement which provides confidence in the other modeling results.

Additionally, observed in Figure 5, serpentines displacement is nonsymmetric about the center axis. Reflected in both model and experiments, the rectangular anchor points connecting the serpentine to the frame are displaced by 55 μm in the y-direction, likely changing the serpentine's center of mass during strain loading. FEA results show under applied external strain the maximum stress occurs within the arcs of the serpentine, therefore it is assumed that the sharp corners at the anchor points should not be the location of fracture. However, if a notch or a crack is introduced into the corner through fabrication it can become susceptible to premature brittle fracture. The twisting and buckling behavior of the structure is not desirable for practical implementation of Si interconnects. This problem can be overcome by increasing Si thickness to a value larger than the width $\left(1 < \frac{t_{Si}}{w_{Si}}\right)$ which promotes in-plane scissoring deformation only.[14,23]

2.3. Stress Characterization with Micro-Raman Spectroscopy

2.3.1. Raman Calibration

To further explore anisotropic effects on Si serpentines, we employ localized stress characterization with μRS on serpentines strain loaded along the <110> and <100> directions. Based on crystal symmetry of the diamond cubic structure, the one longitudinal optical (LO) and two transverse optical phonon modes in Si are triple degenerate, corresponding to a characteristic wavenumber reported to range between w_0 = 520–521 cm^{-1}.[41,42] When the Si crystal is under uniaxial or biaxial strain, the triple degeneracy of the optical phonons are lifted, resulting in a peak broadening and linear wavenumber shift of the Si Raman LO mode ($\Delta\omega_3$).[39–42] De Wolf derived the relationship between stress and shift in the Raman peak position where tensile stress (+σ) shifts the spectra to lower wavenumbers and compressive stress (−σ) to higher wave numbers, shown in Equation (1).[39] As such, relative changes in the Raman wavenumber result in characterization of the crystal's strain state, where a shift of 1 cm^{-1} corresponds to a stress change of 500 MPa, Equation (2).[39]

$$\Delta\omega_3(\mathrm{cm}^{-1}) = \omega_s - \omega_o = -2\times10^{-9}\sigma(\mathrm{Pa}) \quad (1)$$

$$\sigma(MPa) = -500\times\Delta\omega_3\left(\mathrm{cm}^{-1}\right) \quad (2)$$

Here, the Raman linear shift ($\Delta\omega_3$) is the change in the wavenumber between the reference sample (ω_0) and the serpentine (ω_s). For calibration purposes we use Raman and X-ray diffraction (XRD) to determine if fabrication induces stress onto the device layer of the SOI. In this case, ω_0 is peak position of the Si LO mode in the SOI sample as grown, and ω_s is the position of the SOI after processing with backside DRIE. **Figure 6**a shows the Raman spectra of the as-grown reference sample displaying a primary LO peak at w_0 = 521.96 cm^{-1}, and a secondary Si peak at 950 cm^{-1}. Figure 6b shows a shift in the as-grown SOI (black) LO mode wavenumber from ω_o = 521.96 cm^{-1} to ω_s = 521.86 cm^{-1} from backside DRIE etching (red). Using Equation (2), this Raman shift corresponds to an overall low tensile stress of 50 MPa, within the experimental resolution of the instrument (≈0.1 cm^{-1} or +/−50 MPa). XRD measurements were employed to confirm there was negligible change in the crystallinity and stress state of the SOI reference sample before and after etching. Figure 6c shows a Si (004) 2theta-omega (2θ–ω) line scan recorded for the as-grown (black) and DRIE processed SOI (red). The scans exhibit a shift of 0.001° in the 2θ peak position due to processing, which is close to the resolution limit of the diffractometer (0.003°). The lack of a significant shift in 2θ value indicates no change in strain state due to DRIE processing, complementary to Raman observations.

2.3.2. Raman Stress Measurements on Serpentines

Raman stress measurements were then performed on Si serpentines under anisotropic loading conditions using the same sample holder previously described. With assistance of a motorized XY stage, it was possible to define a XY coordinate map to track and measure the same positions on the serpentines precisely after applied cyclic strain. To evaluate anisotropic effects on the maximum and minimum stress concentrations positions, Raman spectra are taken along several positions in straight lines across the width of the serpentine traces. The positions measured on <110> and <100> serpentines are located at the center of the arc (amplitude), off-center of the arc (bend), and along the long parts of serpentine (straight), as described in the experimental methods and shown in Figure S4a–c in the Supporting Information.

A <110> serpentine was pulled to a 40% maximum local strain within the 3rd (middle) period which corresponds to a 17% global strain, as shown in Figure S4d in the Supporting Information. **Figure 7**a shows the resulting stress concentrations collected from the line scans on the amplitude, bend, and straight, revealing maximum stress concentration occurs at the apex of the amplitude for serpentines strained loaded along the <110> direction. The maximum stress at the apex of the amplitude is shown to be 1.9× larger for serpentines strain loaded along the <110> direction, compared to the <100> direction, consistent with modeling results. As expected from prior work, the minimum stress occurs along the straight segment of the serpentine which agrees well with predictions from the 3D models.

The <100> serpentine shown in Figure 5b was pulled to a maximum strain value of 76%, returned to equilibrium (0%), and then cycled to a local strain of 0–40% 15 times manually. In the case of a <100> serpentine, a maximum local strain of 40% in the 3rd (middle) period corresponds to a global strain

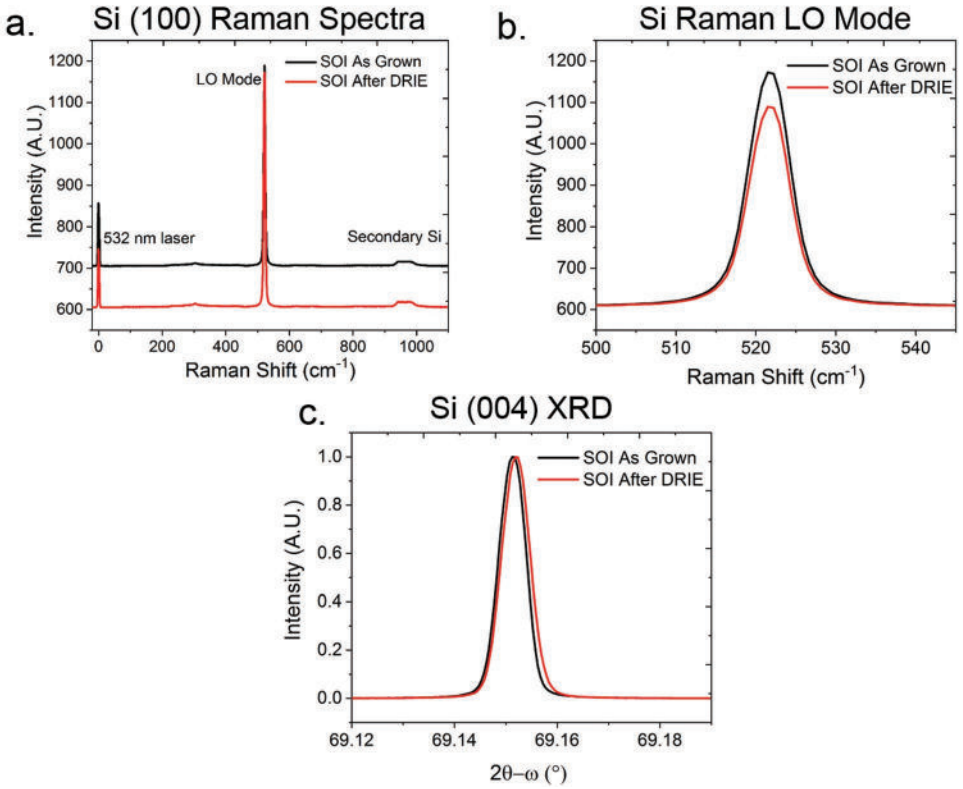

Figure 6. Effect of backside DRIE etching on the stress distribution within the device SOI film. a) Raman Spectra of (100) SOI wafer. b) Raman LO peaks of the unstressed state ($\omega_0 = 521.96$ cm^{-1}) (black), and after DRIE on the handle layer (red) ($\omega_s = 521.86$ cm^{-1}). c) 2θ-ω XRD scan of the (004) reflection of the SOI film as grown (black) and after DRIE etching (red) showing a negligible 2θ-ω shift of 0.001°.

of 30%, shown in Figure S4e in the Supporting Information. Figure 7b–d shows the stress fatigue behavior for cycles 1,5,10, and 15 on the amplitude, bend, and straight sections of the <100> serpentine, at a local strain of 40%. In good agreement with FEA results, the maximum stress concentrates near the bend of the <100> serpentine most likely due to out-of-plane buckling deformation and resulting shear stresses in the <110> direction in that area. During Raman measurements, only 40 µm of the serpentine width of the straight segment was in focus. It was evident there was severe twisting deformation based on a *z*-height focus change of 150 µm between the amplitude and straight segment. The other 15 µm of width were hidden from view due to the limited field of view of the microscope. Figures 7a,c, both show the straight part of the serpentine trace is found to consistently concentrate the minimum stress in both the Raman experiments and in the models, regardless of crystal orientation. Error in the measurements could potentially arise from slight position misalignment which would promote multiaxis deformation. With applied cyclic strain, there was a baseline small shift of 100–200 MPa. The lack of significant change in stress state between the first and last cycle indicates that Si serpentine deformation is highly elastic.

Upon evaluation of the maximum stress and eventual fracture location of the <110> and <100> serpentines, we find fracture will occur at the weakest point of the geometrical architecture which intersects the <110> Si slip direction. In agreement with the FEA modeling predictions, Figure 7a Raman measurements confirmed the maximum stress in the <110> serpentine occurred at the apex, while Figure 7c, shows the maximum stress in the <100> serpentine occurs along the bend. In the case of the 55 µm wide curved corner serpentines, the fracture point is expected to occur at the apex of the amplitude for <110> devices, whereas the fracture location for the <100> device occurs off-center at the bend. Experimental and theoretical modeling evidence of anisotropic effects on the serpentine fracture locations are shown in **Figure 8**. Since fracture is observed to occur along the <110> direction, it is recommended to strain load serpentines along this direction to ensure optimal mechanical performance and device stability.[32]

3. Conclusion

In summary, we model and experimentally demonstrate the effects of crystalline anisotropy on the mechanical stretchable behavior of in-plane single crystal silicon serpentines. Through FEA we demonstrate anisotropic strain variations within the (100) Si plane of up to 20% with the <100> direction being the most stretchable. The Si (111) plane displays the <110> direction and is modeled to reach maximum tensile strains 14–21% lower than those patterned parallel to the <100> direction. We develop a fabrication process that allows for the release of stress-free stretchable in-plane Si (100) serpentines

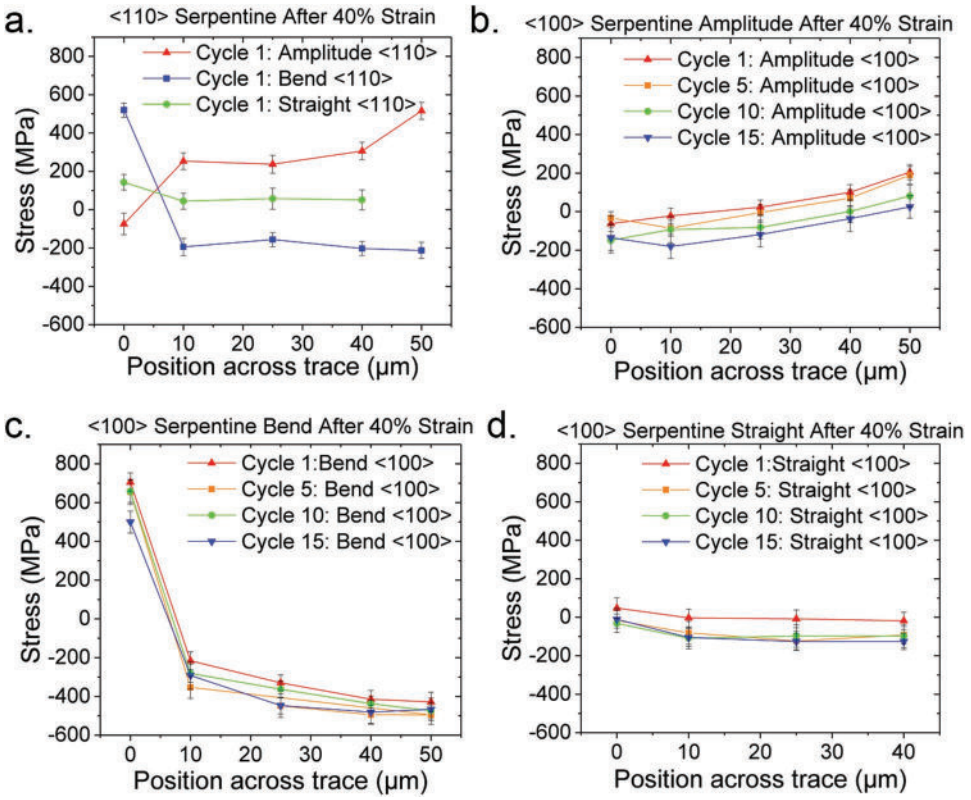

Figure 7. Stress monitoring of serpentine maximum stress concentration position with μRS. Stress as a function of position across the width of the serpentine trace (μm) on a) the amplitude, bend, and straight part of a <110> serpentine after a 40% local strain. Stress fatigue monitoring of the stress changes on a <100> serpentine after a 40% local strain within the b) Amplitude c) Bend, and d) Straight segments at cycle 1, 5, 10, and 15. The error bars represent the uncertainty in the peak fitting of the Raman measurement.

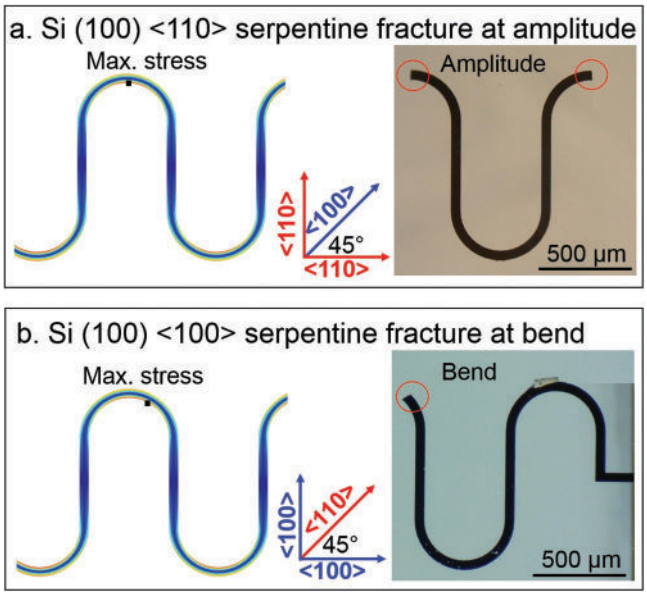

Figure 8. Model and experimental comparison of anisotropic effects on fracture location of in-plane curved corner serpentines with a 55 μm width. a) The maximum stress and fracture location of serpentines parallel to the <110> direction occur in the amplitude while b) maximum stress and fracture in the <100> direction occurs in the bend.

aligned in the <110> and <100> directions, for mechanical testing. Mechanical tensile tests and FEA results demonstrate reasonable agreement for the global and local strain displacement profiles of w = 55 μm <110> and <100> serpentines. Raman spectroscopy stress experiments coupled with low-cycle straining, are employed to study anisotropic effects of the maximum stress concentration of identical serpentine geometries patterned in the <110> and <100> direction. Raman measurements confirm the maximum stress on the serpentine will always align in the <110> direction, demonstrated by different fracture locations at the amplitude and bend for <110> and <100> serpentines, respectively.

While there are many anisotropic semiconductors, the scope of this paper was focused only on single crystal Si. There are still many areas to be explored before the community fully understands anisotropic effects in stretchable semiconductors. Potential future work that would be beneficial include fabricating and demonstrating Si serpentine devices in the <100> direction can reach larger strains than the <110> direction. Additionally, experimental demonstrations of serpentines from Si (111) still needs to be complete. Understanding and compensating for anisotropic effects in stretchable semiconductors is critical for the further development of reliable, stretchable electronic technologies. The anisotropic modeling, fabrication, and characterization procedures reported here for silicon, are adaptable to other stretchable, anisotropic, inorganic semiconductors.

4. Experimental Section

Finite Element Analysis: A 3D Structural Mechanics Linear Elastic COMSOL Multiphysics 5.3 model was employed to analyze uniaxial serpentine deformation. In-plane Si curved corner serpentines with the following dimensions were considered: A = 1 mm, λ = 1 mm, r = 250 μm arc radius, w = 25–100 μm. The 3D geometries were composed of mesh with domain element sizes ranging between 53143 and 450177. The 3D model is able to solve for out of plane buckling and twisting deformation, which is not possible in 2D solvers.

Fabrication of In-Plane Si Serpentines: Shown in Figure 3, conventional photolithography and a series of plasma etches were used to fabricate <110> and <100> in-plane Si serpentines from a doubled sided polished (100) SOI wafer (University Wafers, device Si 7 μm, buried oxide 2 μm, handle Si 350 μm) (Figure 3a). A 2 μm SiO_2 hard mask was deposited onto the handle wafer using plasma enhanced chemical vapor deposition (PECVD, Plasma Therm 790+). AZ 5214 (MicroChemicals) photoresist was spin coated (3000 rpm, 60 s), soft baked (110 °C, 60 s), exposed through the first photomask, and then developed to define the mechanical support structure. ICP-RIE (Plasma Therm VLR) was used to anisotropically etch the SiO_2 dielectric hard mask pattern. SiO_2 acts as a hard-masking material to Si during DRIE (Plasma Therm 770). In turn, Si is a chemically resistant material during ICP dielectric etching processes to remove SiO_2. The photoresist etch mask was then removed with acetone, methanol, and isopropanol baths, followed by exposure to a low-power O_2 plasma to remove any residual photoresist. This series of photolithography and etching steps were repeated to backside align the second photomask to create a 0.1 μm SiO_2 hard mask pattern consisting of a mechanical support structure with a suspended serpentine onto the device Si (Figure 3b).

The device side of the SOI wafer was mounted onto a 4 in carrier wafer with thermal grease. The handle Si wafer was anisotropically etched via DRIE for 1.5 h with the following parameters: RF power of 850 W, cycling C_4F_8/SF_6/Argon (70/0.5/40 sccm) gas on for 4 s to passivate and C_4F_8/SF_6/Argon (0.5/100/40 sccm) gas on for 6 s to etch. The exposed oxide layer was then fully removed with an ICP dielectric etch (Figure 3c). The sample was separated from the carrier wafer, cleaned, and remounted onto the carrier wafer, handle Si down. The device Si was subjected to DRIE for 4 min to fully release the serpentine structure (Figure 3d). The fabricated piece was then removed from the carrier and subjected to a mild O_2 plasma to remove any organic residue. The final released structure was stripped of any remaining SiO_2 using a 30 min clean to isotropic vapor hydroflouric acid (Primaxx HF Etcher).

Testing Holder Stage: A custom built sample holder allowed controlled mechanical stretching and compressing of the serpentines while mounted onto the XY motorized stage under the Raman microscope. The short edges of the 3 × 7 mm mechanical frame supporting the released serpentine were fixed onto two microscope slides mounted into the holder via epoxy, Figure S2b in the Supporting Information. The long sides of the frame were breakaway regions, cut prior to serpentine straining, shown in Figure S2c in the Supporting Information. Optical microscopy with a Keyence VHX 6000 Microscope with a 200× objective lens was used to measure global end-to-end displacements and local strain within the period. SEM images were taken using a Zeiss AURIGA SEM.

Micro Raman Spectroscopy: A WITec Alpha300RA confocal Raman Microscope using a Nd:YAG 1064 μm frequency doubled excitation laser source (532 nm, 0.5 mW) focused through a Zeiss 100× long working distance microscope objective lens with a high spatial resolution of 300 nm. Single Raman spectra were collected in the (001) backscattered geometry of Si, with 0.5 s integration time through a 1800 g mm^{-1} grating spectrometer. Si Raman peaks were fit using a Lorentzian function (resolution of fit is 0.1 cm^{-1} or 50 MPa based on Equation (2)).

Our instrument was paired with a motorized XY stage, which allowed to define a coordinate system to track the measurement positions. After each strain cycle, it was possible to precisely measure the same locations of the serpentine. Raman spectra were collected in 10–15 μm steps along a 55 μm wide cross section of the center of the arc (amplitude), and off-center of the arc (bend) on the serpentines after applying a local 40% strain within the period, using the custom-built sample holder previously described. A 40 μm wide cross section was obtained along the straight section of the serpentine due to observed out-of-plane twisting, resulting in a detected change in z-height focus of the microscope up to 150 μm between the amplitude and the straight sections. The origin (0, 0) μm was located precisely at the top centered edge of amplitude on the 3rd (middle) period in the 5-period serpentine trace and served as the reference position for the measurements (Figure S4a, Supporting Information). The bend was at a location ≈(50, −120) μm away from the amplitude (Figure S4b, Supporting Information). The straight location was of ≈(500, −500) μm (Figure S4c, Supporting Information). The serpentine was stretched to a local strain of 40% in the 3rd (middle) period, compressed back to equilibrium (0%), and stretched again to a local strain of 40% for one complete cycle. The origin was redefined back to (0, 0) μm after each cycle, repeated up to 15 times for cyclic Raman measurements.

X-Ray Diffraction: Raman stress calculations were confirmed using high resolution XRD measurements recorded on a PANalytical X'Pert materials research diffractometer. The system was equipped with an X-ray tube source in line focus mode collimated for a single wave length Cu Kα_1 radiation (λ = 1.540498 Å) using a parabolic W/Si multilayer mirror and a symmetric Ge (220) four-bounce monochromator. A symmetric Ge (220) three-bounce analyzer crystal was placed in front of a Xe proportional detector to limit the 2θ angular acceptance range to 0.003°.

Supporting Information

Supporting Information is available from the Wiley Online Library or from the author.

Acknowledgements

S.M.C. would like to thank H. Wang for his advice on anisotropic FEA modeling. S.M.C. and M.B.G. acknowledge support sponsored by the Army Research Laboratory accomplished under Cooperative Agreement Number W911NF-17-2-0063. The views and conclusions contained in this document are those of the authors and should not be interpreted as representing the official policies, either expressed or implied, of the Army Research Laboratory or the U.S. Government. The U.S. Government is authorized to reproduce and distribute reprints for Government purposes notwithstanding any copyright notation herein.

Conflict of Interest

The authors declare no conflict of interest.

Keywords

anisotropy, micro-Raman spectroscopy, serpentine, silicon, stretchable semiconductor

Received: December 29, 2018
Revised: February 26, 2019
Published online: May 2, 2019

[1] J. A. Rogers, T. Someya, Y. Huang, *Science* **2010**, *327*, 1603.
[2] D.-H. Kim, N. Lu, R. Ma, Y.-S. Kim, R.-H. Kim, S. Wang, J. Wu, S. M. Won, H. Tao, A. Islam, K. J. Yu, T-i. Kim, R. Chowdhury, M. Ying, L. Xu, M. Li, H.-J. Chung, H. Keum, M. McCormick, P. Liu,

Y.-W. Zhang, F. G. Omenenetto, Y. Huang, T. Coleman, J. A. Rogers, *Science* **2011**, *333*, 838.
[3] W.-H. Yeo, Y.-S. Kim, J. Lee, A. Ameen, L. Shi, M. Li, S. Wang, R. Ma, S.-H. Jin, Z. Kang, Y. Huang, J. A. Rogers, *Adv. Mater.* **2013**, *25*, 2773.
[4] D.-H. Kim, N. Lu, Y. Huang, J. A. Rogers, *MRS Bull.* **2012**, *37*, 226.
[5] D.-H. Kim, Z. Liu, Y.-S. Kim, J. Wu, J. Song, H. S. Kim, Y. Huang, K. C. Hwang, Y. Zhang, J. A. Rogers, *Small* **2009**, *5*, 2841.
[6] J. Lee, J. Wu, J. H. Ryu, Z. Liu, M. Meitl, Y. W. Zhang, Y. Huang, J. A. Rogers, *Small* **2012**, *8*, 1851.
[7] R. C. Webb, A. P. Bonifas, A. Behnaz, Y. Zhang, K. J. Yu, H. Cheng, M. Shi, Z. Bian, Z. Liu, Y. S. Kim, W. H. Yeo, *Nat. Mater.* **2013**, *12*, 938.
[8] T. Someya, T. Sekitani, S. Iba, Y. Kato, H. Kawaguchi, T. Sakurai, *Proc. Natl. Acad. Sci. U. S. A.* **2004**, *101*, 9966.
[9] Y. M. Song, Y. Xie, V. Malyarchuk, J. Xiao, I. Jung, K. J. Choi, Z. Liu, H. Park, C. Lu, R. H. Kim, R. Li, *Nature* **2013**, *497*, 95.
[10] B. Balakrisnan, A. Nacev, J. M. Burke, A. Dasgupta, E. Smela, *Smart Mater. Struct.* **2012**, *21.7*, 075033.
[11] N. Lazarus, C. D. Meyer, S. S. Bedair, *IEEE Trans. Electron Devices* **2015**, *62*, 2270.
[12] D. S. Gray, J. Tien, C. S. Chen, *Adv. Mater.* **2004**, *16*, 393.
[13] Y. Zhang, S. Wang, X. Li, J. A. Fan, S. Xu, Y. Min Song, K.-J. Choi, W. H. Yeo, W. Lee, S. Nafees Nazaar, B. Lu, L. Yin, K.-C. Hwang, J. A. Rogers, Y. Huang, *Adv. Funct. Mater.* **2014**, *24*, 2028.
[14] Y. Su, X. Ping, K. Yu, J. Lee, J. Fan, B. Wang, M. Li, R. Li, D. Harburg, Y. Huang, C. Yu, S. Mao, J. Shim, Q. Yang, P. Lee, A. Armonas, K. Choi, Y. Yang, U. Paik, T. Chang, T. Dawidczyk, Y. Huang, S. Wang, J. Rogers, *Adv. Mater.* **2017**, *29*, 1604989.
[15] T. Widlund, S. Yang, Y.-Y. Hsu, N. Lu, *Int. J. Solids Struct.* **2014**, *51*, 4026.
[16] N. Lu, X. Wang, Z. Suo, J. Vlassak, *Appl. Phys. Lett.* **2007**, *91*, 221909.
[17] T. Pan, M. Pharr, Y. Ma, R. Ning, Z. Yan, R. Xu, X. Feng, Y. Huang, J. Rogers, *Adv. Funct. Mater.* **2017**, *27*, 1702589.
[18] Z. Xue, T. Dong, Z. Zhu, Y. Zhao, Y. Sun, L. Yu, *J. Semicond.* **2018**, *39*, 011001.
[19] F. Xu, W. Lu, Y. Zhu, *ACS Nano* **2011***5*, 672.
[20] I. Mahaboob, K. Hogan, S. W. Novak, F. Shahedipour-Sandvik, R. P. Tompkins, N. Lazarus, *J. Vac. Sci. Technol., B: Nanotechnol. Microelectron.: Mater., Process., Meas., Phenom.* **2018**, *36*, 031203.
[21] I. Mahaboob, J. Marini, K. Hogan, E. Rocco, R. P. Tompkins, N. Lazarus, S. Shahedipour-Sandvik, *J. Electron. Mater.* **2018**, *47*, 6625.
[22] R. P. Tompkins, I. Mahaboob, F. Shahedipour-Sandvik, N. Lazarus, *Solid-State Electron.* **2017**, *136*, 36.
[23] B. Wang, S. Bao, S. Vinnikova, P. Ghanta, S. Wang, *npj Flexible Electron.* **2017**, *1*, 5.
[24] J. H. Lee, J. P. Singer, E. L. Thomas, *Adv. Mater.* **2012**, *24*, 4782.
[25] A. Alderson, K. L. Alderson, *Proceedings of the Institution of Mechanical Engineers, Part G: Journal of Aerospace Engineering*, **2007**, *221*, 565.
[26] D. J. Lipomi, Z. Bao, *Energy Environ. Sci.* **2011**, *4*, 3314.
[27] A. Muslija, A. D. Lantada, *Smart Mater. Struct.* **2014**, *23*, 087001.
[28] R. R. A. Syms, D. Liu, M. M. Ahmad, J. Micromechanics, *J. Micromech. Microeng.* **2017**, *27*, 075003.
[29] A. Chortos, J. Lim, J. To, M. Vosgueritchian, T. Dusseault, T. Kim, S. Hwang, Z. Bao, *Adv. Mater.* **2014**, *26*, 4253.
[30] O. M. Awartani, B. Zhao, T. Currie, R. J. Kline, M. A. Zikry, B. T. O'Connor, *Macromolecules* **2016**, *49*, 327.
[31] S. E. Root, S. Savagatrup, A. D. Printz, D. Rodriquez, D. J. Lipomi, *Chem. Rev.* **2017**, *117*, 6467.
[32] D. McCarter, R. A. Paquin, *presented at Proc. SPIE, Material Technologies and Applications to Optics, Structures, Components, and Sub-Systems*, San Francisco, CA, September **2013**, *8837*, 883707.
[33] J. Y. Huang, J. W. Huang, T. Sun, K. Fezzaa, S. L. Xu, S. N. Luo, *Acta Mater.* **2016**, *114*, 136.
[34] J. Song, *Appl. Phys. Lett.* **2010**, *96*, 051913.
[35] R. P. Tompkins, I. Mahaboob, F. Shahedipour-Sandvik, N. Lazarus, *ECS Trans.* **2016**, *72*, 89.
[36] M. A. Hopcroft, W. D. Nix, T. W. Kenny, *J. Microelectromech. Syst.* **2010**, *19*, 229.
[37] E. Anastassakis, A. Pinczuk, E. Burstein, F. H. Pollak, M. Cardona, *Solid State Commun.* **1970**, *8*, 133.
[38] T. Englert, G. Abstreiter, J. Pontcharra, *Solid-State Electron.* **1980**, *23*, 31.
[39] I. DeWolf, *Semicond. Sci. Technol.* **1996**, *11*, 139.
[40] A. Atkinson, S. C. Jain, *J. Raman Spectrosc.* **1999**, *30*, 885.
[41] V. T. Srikar, A. K. Swan, M. S. Ünlü, B. B. Goldberg, S. M. Spearing, *J. Microelectromech. Syst.* **2003**, *12*, 779.
[42] L. Starman, R. Coutu, *Exp. Mech.* **2012**, *52*, 1341.
[43] M. Kuball, *Surf. Interface Anal.* **2001**, *31*, 987.
[44] F. Cerdeira, C. J. Buchenauer, F. H. Pollak, M. Cardona, *Phys. Rev. B* **1972**, *5*, 580.
[45] K. M. Knowles, P. R. Howie, *J. Elasticity* **2015**, *120*, 87.
[46] J. J. Wortman, R. Evans, *J. Appl. Phys.* **1965**, *36*, 153.
[47] J. Kim, D. D. Cho, R. S. Muller, presented at *Transducers' 01 Eurosensors XV*, Springer, Munich, Germany **2001**, 662.
[48] L. Zhang, R. Barrett, P. Cloetens, C. Detlefs, M. Sanchez del Rio, *J. Synchrotron Radiat.* **2014**, *21*, 507.
[49] S. Choi, K. Y. Jhang, *Appl. Phys. Lett.* **2014**, *104*, 251604.
[50] K. E. Petersen, *Proc. IEEE* **1982**, *70*, 420.